



Heat budget responses of the eastern China seas to global warming in a coupled atmosphere–ocean model

Di Tian¹, Jian Su^{2,3,*}, Feng Zhou^{1,4}, Bernhard Mayer², Dmitry Sein^{5,6}, Han Zhang^{1,7},
Daji Huang^{1,4}, Thomas Pohlmann²

¹State Key Laboratory of Satellite Ocean Environment Dynamics, Second Institute of Oceanography,
Ministry of Natural Resources, Hangzhou 310012, PR China

²Institute of Oceanography, Centre for Earth System Research and Sustainability, University of Hamburg, Hamburg 20146, Germany

³Danish Meteorological Institute, Lyngbyvej 100, Copenhagen 2100, Denmark

⁴Ocean College, Zhejiang University, Zhoushan 316021, PR China

⁵Alfred Wegener Institute for Polar and Marine Research, Am Handelshafen 12, Bremerhaven 27570, Germany

⁶Shirshov Institute of Oceanology, Russian Academy of Science, Moscow 117218, Russia

⁷Southern Marine Science and Engineering Guangdong Laboratory (Zhuhai), Zhuhai 519082, PR China

ABSTRACT: The impacts of climate change on the heat budget of the eastern China seas (ECSs) are estimated under the historical representative concentration pathway (RCP) 4.5 and RCP8.5 scenarios using an atmosphere–ocean coupled regional climate model system (REMO/MPIM). The results suggest that recent and future ocean warming over the ECSs is linked overall to increased oceanic heat transport by currents, which is partly compensated by air–sea heat exchange. The Taiwan Strait is the major source of oceanic heat for the ECSs, whereas the shelf break section (SBS) acts as a heat sink. An increase in net oceanic heat transport into the ECSs is projected under both considered RCP scenarios, mainly resulting from a reduction of the outward heat transport through the SBS. The mean relative contribution of SBS to the oceanic heat transport thus decreases by 4 to 5 % under both RCP scenarios, relative to the historical run. Regarding the surface air–sea exchange, the heat loss caused by thermal radiation and latent and sensible heat in the ECSs exceeds the heat gain achieved by solar radiation. Under the RCP scenarios, warmer sea surface temperature and stronger surface wind will enhance the upward latent heat flux, eventually leading to a more pronounced heat loss from the ECSs. The mean relative contributions of the latent heat flux to the air–sea heat exchange notably increases by 2 to 3 % under both projection scenarios, relative to the historical run. Taking into account all components of the heat balance of the ECSs, we deduce that the increased horizontal heat transport will enhance the surface evaporation over the ECSs under future warming.

KEY WORDS: Climate projections · Air–sea heat flux · Oceanic heat transport · Ocean heat budget · Regional climate modeling · Climate change impacts

1. INTRODUCTION

Changes in the ocean heat budget, predominantly revealed by the anomalies of ocean temperature and ocean heat content (OHC), are crucial to global and regional climate and weather systems (Yang et al. 2007). Simultaneously, heat budget changes play a fundamental role in ocean processes (e.g. circulation, stratification; Toggweiler & Russell 2008, Keeling et

al. 2010) and marine ecosystems (Harley et al. 2006, Wernberg et al. 2013). Global OHC has increased considerably over the last half century, with substantial superimposed temporal variability (Levitus et al. 2000, Domingues et al. 2008, Levitus et al. 2012, IPCC 2013, Cheng et al. 2017). During the period from 1971 to 2010, >90 % of the net energy increase in the climate system was stored in the ocean, mainly through the air–sea heat exchange (IPCC 2013, Sec-

*Corresponding author: jis@dmi.dk

tion B.2 Ocean of Summary for Policymakers). Ocean warming is not uniformly distributed. The coastal ocean has suffered a more notable warming than the open ocean in recent decades, causing a severe impact on coastal marine ecosystems (Belkin 2009, Gilbert et al. 2010, Huang et al. 2012, Lima & Wethey 2012, Wu et al. 2012, Breitburg et al. 2018).

The regions of interest for this study are the eastern China seas (ECSs), which lie between China, Korea and Japan, from approximately 24° to 42° N and from 117° to 130° E (Fig. 1). The ECSs include 3 marginal seas (from north to south): Bohai Sea, Yellow Sea and East China Sea (ECS). The ECSs exhibit one of the widest continental shelves in the world, and have experienced a notable warming trend in the last century (Lin et al. 2001, 2005, Tang et al. 2009, Yeh &

Kim 2010, Huang et al. 2012). The ECSs have complex terrains and unique circulation systems (Ichikawa & Beardsley 2002, Xie et al. 2002, Yuan & Hsueh 2010). Simultaneously, these seas are affected by various sources of forcing, such as the East Asian monsoon (Oey et al. 2013, Huang et al. 2016), Kuroshio Current (Chern et al. 1990, Soeyanto et al. 2014, Wang & Oey 2016), El Niño Oscillation (ENSO); (Park & Oh 2000), Pacific Decadal Oscillation (PDO); (Jung et al. 2017) and other factors. As a result, sea surface temperature (SST) variations over these coastal seas exhibit multiple timescales and spatial patterns (Tseng et al. 2000). Many studies have been performed to interpret the dominant mechanism of the SST change in the ECSs (Kim et al. 2018). Relative to the SST, the OHC is a better indicator for ocean

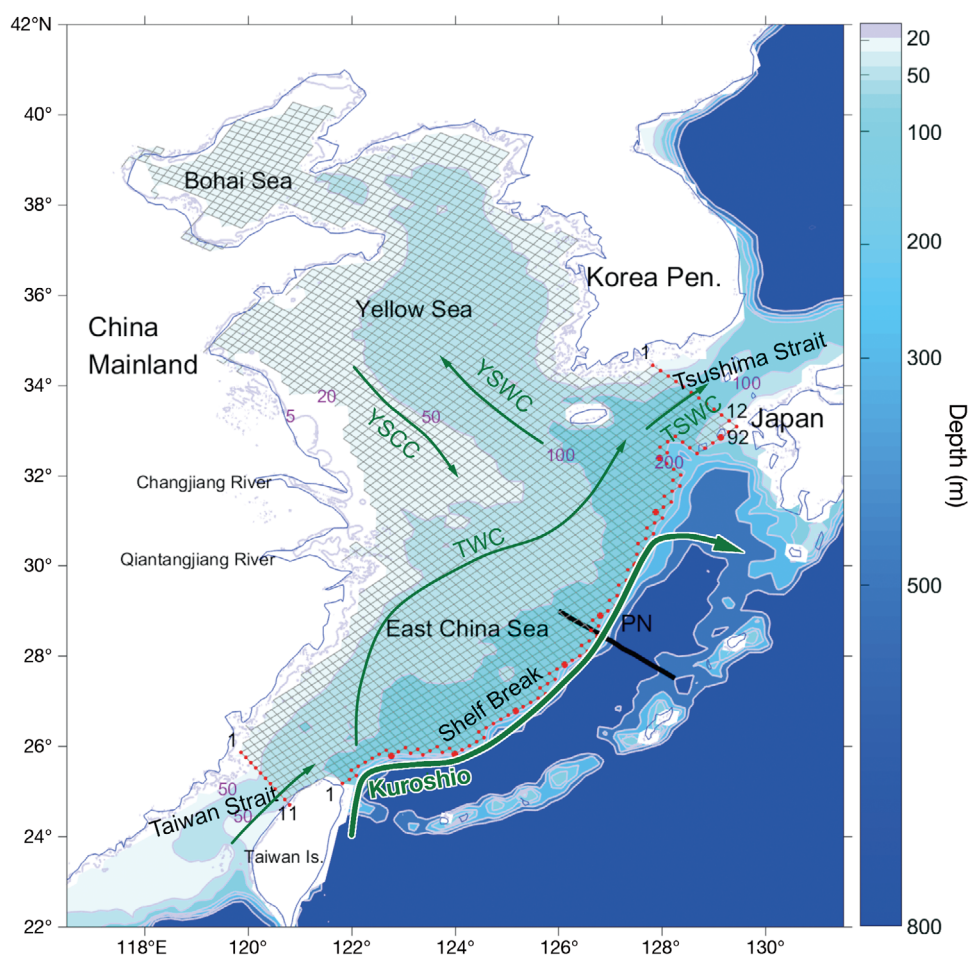


Fig. 1. Model grid and bathymetry in the eastern China seas (ECSs). Regions are designated as follows: the shelf break section (SBS; close to 200 m isobath), the Taiwan Strait (TAS), and the Tsushima Strait (TUS). Contours represent isobaths (i.e. 5, 20, 50, 100, 200, 300, 500, 800 m). Red dots depict sections along the SBS, through the TAS, and through the TUS as employed in this study, with 92, 11, and 12 horizontal grid points, respectively. Larger red dots along the SBS depict 10-point intervals starting from the Taiwan coastline. Black bold line depicts location of the PN section. Solid arrows represent schematic currents in the ECSs: Yellow Sea Coastal Current (YSCC), Yellow Sea Warm Current (YSWC), Taiwan Warm Current (TWC), Tsushima Strait Warm Current (TSWC), and Kuroshio

warming and climate variability, because it also allows for a quantitative assessment of the ocean heat balance. However, there is still a lack of studies that discuss warming of the ECSs from the perspective of the OHC.

Another topic presently under discussion concerns the oceanic heat exchange due to currents in the ECSs (schematic currents are shown in Fig. 1). The Kuroshio, the strong western boundary current in the North Pacific, enters the ECS from northeast of Taiwan, with the main flow extending northeastward along the shelf break. The major Kuroshio onshore intrusions occur northeast of Taiwan and southwest of Kyushu. The mixture water of the intruding Kuroshio water and the Taiwan Strait water, known as the Taiwan Warm Current (TWC), is commonly considered an important source of saline water for the ECS shelf (Su & Pan 1987). The TWC and the Kuroshio intrusion are thought to be the major origins of the Tsushima Warm Current (TSWC; Isobe 1999). Based on observations (Isobe 2008) and regional ocean models (Guo et al. 2006, Isobe & Beardsley 2006, Lee & Takeshi 2007, Song et al. 2011), oceanic volume transport has been widely studied. The most recent estimates, using the Regional Ocean Modeling System (ROMS), give a climatological annual mean volume transport of 1.52 Sv for the Taiwan Strait (TAS), 1.17 Sv for the shelf break section (SBS) and -2.67 Sv for the Tsushima Strait (TUS) of the ECS, showing strong seasonal variations (Zhou et al. 2015). Transport here is defined as positive for incoming fluxes and negative for outgoing fluxes. In addition to seasonal variation, the Kuroshio intrusion onto the southern shelf of the ECS also shows an interannual variability, which is suggested to be related to the ENSO and PDO (Wu et al. 2014), that also can be affected by the Kuroshio volume transport itself (Liu et al. 2014). J. Zhang et al. (2017) further demonstrated that the bottom layer is an important pathway for water exchange of ECS shelf water and the open sea. The oceanic heat transport was also estimated in several studies (Liu et al. 2010, Zhang et al. 2012, Zhou et al. 2015), giving a net heat transport of 0.04 to 0.05 PW into the ECS. Zhang et al. (2012) indicated that the Kuroshio heat transport passing across the PN section (Fig. 1) in the ECS exhibits interannual and interdecadal variability. However, compared with the volume exchange, the heat exchange still attracts less attention, especially the combined effect of the oceanic heat exchange and air–sea heat exchange on the regional ocean heat budget.

Some studies have investigated the changes in the ECSs under climate change scenarios (Sakamoto et

al. 2005, Yu et al. 2012, Seo et al. 2014, Li et al. 2017, X. Zhang et al. 2017). Based on an experiment with an atmospheric CO_2 concentration increasing ideally by $1\% \text{ yr}^{-1}$, Sakamoto et al. (2005) suggested that the Kuroshio Current will be strengthened because of increased recirculation. The same result of the intensified Kuroshio Current under global warming is found in other simulations, such as the Special Report on Emissions Scenarios (SRES) B1, A1B and A2 scenarios, using ROMS (Yu et al. 2012) and the representative concentration pathway (RCP) 4.5 scenario using the high-resolution climate model MIROC4h (X. Zhang et al. 2017, Li et al. 2017). Yu et al. (2012) also noted that SST increases more drastically in the Bohai Sea and central Yellow Sea than along the southeastern coast of China, along the western coast of Korea and in the southern ECS under SRES B1, A1B and A2. Using dynamic downscaling from global climate models, Seo et al. (2014) indicated that heat supply to the atmosphere decreases in most of the Northwest Pacific marginal seas due to a slower warming of the sea surface compared with the atmosphere. In addition, volume transport through major straits, except the TAS, is projected to slightly increase under SRES A1B. However, future projections of the oceanic heat exchange, the air–sea heat exchange and their combined impacts on the heat budget of the ECSs lack research, especially those based on the state-of-the-art climate change scenarios (Moss et al. 2010), which are recommended by the 5th assessment report of the IPCC (IPCC AR5).

We address these aforementioned shortcomings in this study and investigate the current and future changes in the OHC at the ECSs at the basin scale using a zoomed global coupled atmosphere–ocean model. Simultaneously, we will systematically discuss the current and future changes in horizontal advection and air–sea exchange of heat and quantify their relative contributions to the changes in the heat budget of the ECSs. One historical scenario (20C) and 2 RCP scenarios (RCP4.5 and RCP8.5) are used in this study.

2. DATA AND METHODS

2.1. Model description

An atmosphere–ocean coupled model system has been applied in this study. The model system has 3 components: the regional climate model (REMO) as an atmospheric component, the Max Planck Institute ocean model (MPIOM) as an ocean component and OASIS3 as a coupler. The REMO originally devel-

oped by the Max Planck Institute for Meteorology in Hamburg is based on primitive equations in a terrain-following hybrid coordinate system (Jacob & Podzun 1997). The REMO model is transferable and has been identified as well suited for long-term climate change simulations to examine projected regionalized future changes (Jacob et al. 2012). The MPIOM (Jungclaus et al. 2013) is the ocean–sea ice component of the Max Planck Institute for Meteorology Earth System Model (MPI-ESM), which joins the Coupled Model Intercomparison Project Phase 5 (CMIP5; Taylor et al. 2012, Giorgetta et al. 2013). MPIOM is a free-surface ocean general circulation model formulated on an Arakawa C-grid and a z-coordinate system in the vertical direction. The details of model equations and physical parameterizations can be found in Marsland et al. (2003). In this coupled model system, the MPIOM needs to be run in both coupled and stand-alone modes simultaneously, since the REMO covers only a part of the global ocean. Through the coupler OASIS3, the MPIOM model running in the coupled subdomain receives the heat, freshwater and momentum fluxes calculated in REMO at a specified frequency (coupling time step) and passes the sea surface conditions to the atmospheric model. In the uncoupled subdomain, the MPIOM model calculates heat, freshwater and momentum fluxes from the global, predefined atmospheric fields (e.g. from reanalysis data) using bulk formulas at a specified frequency (forcing time step). The more detailed model description of REMO/MPIOM can be found in Sein et al. (2015).

Note that the MPIOM version used in this study is a zoomed global setup, reallocating 2 poles on the Euro-Asian continent and Australia to assure high resolution in the western Pacific. The advantage of such a zoomed method compared with the traditional nesting method is that it can avoid open boundary effects (Su et al. 2014), which is essential in the ECSs. The horizontal resolution for the MPIOM is approximately 0.2° (approximately 20 km) over the western Pacific. This model has 40 uneven vertical levels with increasing level thickness. The MPIOM computational grid and atmospheric model domain used in this study are presented in Fig. 27c of Sein et al. (2015). The coupled subdomain is approximately from 20° S to 45° N and from 65° to 185° E.

2.2. Experiment and data

The REMO/MPIOM model was simulated for 3 periods by taking the initial and open conditions

from a global simulation with the MPI-ESM low-resolution version: (1) 20C historical simulation (1850–2005); note that only 1970–2005 is shown in this study since a period of at least 30 yr is commonly used as a reference period. (2) RCP4.5 future projection (2006–2099) forced by the midrange mitigation emission scenario (RCP4.5) according to IPCC AR5. (3) RCP8.5 future projection (2006–2099) forced by the high-emission scenario (RCP8.5) according to IPCC AR5. In these cases, the computational grid of the REMO has about 55 km horizontal resolution (approximately 0.5°) and 31 hybrid vertical levels. The coupling time step is 3 h.

In this study, to validate the model, REMO/MPIOM also conducted 3 hindcast simulations for the years 1980–2012 by taking the initial and open conditions from the ERA-Interim dataset. See the Supplement at www.int-res.com/articles/suppl/c079p109_supp.pdf for detailed descriptions to these 3 experiments. The multi-member runs can provide additional information on model uncertainties. In addition, OISST (Optimum Interpolation Sea Surface Temperature, daily data from September 1981 to February 2018, <https://www.ncdc.noaa.gov/oisst/data-access>, accessed 8 Aug 2018), the climatological SST field from WOA13 (World Ocean Atlas 2013 version 2, <https://www.nodc.noaa.gov/OC5/woa13/woa13data.html>, accessed 11 Aug 2018), the surface current data achieved from AVISO (Archiving Validation and Interpretation of Satellite Data in Oceanography, daily data from January 1993 to December 2017, <http://icdc.cen.uni-hamburg.de/1/daten/ocean/ssh-aviso/>, accessed 8 Aug 2018) and the near-surface current data from OSCAR (Ocean Surface Current Analyses Real-time, from October 1992 to December 2017; ESR 2009) are used to evaluate the model's performance on the ECSs region. See the Supplement for details of the model validation.

In this study, all oceanic and atmospheric variables from REMO/MPIOM are monthly mean outputs. To be consistent, we interpolate the REMO data onto the MPIOM grid. Surface fluxes are defined as positive into the ocean and negative out of the ocean, and the flows across the open lateral boundaries (OLBs) of the ECSs are defined as positive inward and negative outward.

2.3. Method

To calculate the change in vertically integrated OHC (Δ HC) for each horizontal grid cell, we use the following equation:

$$\Delta \text{HC}_{i,j,t} = \sum_{k=1}^N c_{p(k)} \rho_{(k)} s_h z_{(k)} \Delta T_{(k)} \quad (1)$$

where i and j are position indices in the meridional and zonal directions, respectively; t is the time index; N is the number of layers; $c_{p(k)}$ (heat capacity of seawater) and $\rho_{(k)}$ (density of seawater) are functions of the seawater's salinity, temperature and pressure at layer k ; s_h is the horizontal grid area; $z_{(k)}$ is the thickness of layer k considering changes in the sea surface; and $\Delta T_{(k)}$ is the temperature difference between 2 adjacent time steps. Parameters c_p , ρ , s_h , z and ΔT vary with space and time.

The heat budget method is applied to identify the heat sources of the ECSs, as follows:

$$Q_T = Q_{LB} + Q_{SF} \quad (2)$$

$$Q_{SF} = Q_S + Q_L + Q_{LH} + Q_{SH} \quad (3)$$

where Q_T is the total net heat gain or loss of the ECSs and Q_{LB} is the net heat gain or loss due to the advective heat transport through the OLBs. For the ECSs, 3 OLBs are distinguished (Fig. 1, dotted lines), i.e. the SBS approximated by the 200 m isobath, the TAS (less than 100 m) and the TUS (less than 200 m). These 3 boundaries fully enclose the ECSs. The advective transport of heat between the shelf of the ECS and the open ocean was calculated along these OLBs. Q_{SF} is the net heat gain or loss due to the surface air-sea heat exchange; Q_S , Q_L , Q_{LH} and Q_{SH} are the heat gain or loss by shortwave radiation, longwave radiation, latent heat flux and sensible heat flux, respectively. Heat gain terms are positive, and heat loss terms are negative. Other sources such as river input and net precipitation (the difference between evaporation and precipitation) are small, about 2 orders of magnitude smaller than the ocean advection (Zhou et al. 2015), and therefore not considered in this study.

To calculate the vertically integrated volume transport (VT) and heat transport (HT) across the i^{th} grid point along a section (Fig. 1), we use the following equations:

$$VT_{(i,t)} = \sum_{k=1}^N V_{(k)} s_{v(k)} \quad (4)$$

$$HT_{(i,t)} = \sum_{k=1}^N c_{p(k)} \rho_{(k)} T_{-a(k)} s_{v(k)} \quad (5)$$

where N is the number of layers, $V_{(k)}$ is the velocity component perpendicular to this vertical grid cell of layer k and $s_{v(k)}$ is the vertical area of the corresponding grid cell. $T_{-a(k)}$ is the temperature anomaly relative to the reference temperature [$T_{\text{ref}(k)}$] of layer k . Herein, T_{ref} is determined to be the domain's average temperature of each layer, similar to some previous studies (Kim et al. 2004, Lee et al. 2004) in which

the reference temperature refers to the volume average temperature. Parameters c_p , ρ , T_a , V and s_v are unevenly distributed over the lateral boundary and vary with time. Note that we prefer to use T_{-a} , not temperature (T) adopted by some previous studies (Liu et al. 2010, Zhou et al. 2015), since the former can reflect the impact of water transport through the lateral boundary on the average temperature (or heat content) of a subjected domain in each layer.

To calculate the area averaged surface heat fluxes ($\overline{\text{SHF}}$), we use the following equations:

$$\overline{\text{SHF}} = \sum_{i=1}^M \sum_{j=1}^L \text{SHF}_{(i,j)} R_{(i,j)} \quad (6)$$

$$R_{(i,j)} = A_{(i,j)} / \left(\sum_{i=1}^M \sum_{j=1}^L A_{(i,j)} \right) \quad (7)$$

where M and L are horizontal grid numbers in 2 orthogonal directions, SHF is surface heat flux and R is the ratio of each grid area A to the total area of the ECSs.

To calculate the annual relative contribution (RC) and the multi-annual mean relative contribution ($\overline{\text{RC}}$) of each heat flux component to the total heat flux for oceanic heat transport or air-sea heat exchange, respectively, we use the following equations:

$$\text{RC}_{i,j} = \left(C_{i,j} / \sum_{i=1}^{i=n} |C_{i,j}| \right) \times 100 \quad (8)$$

$$\overline{\text{RC}}_i = \left(\sum_{i=1}^{i=n} \text{RC}_{i,j} \right) / m \quad (9)$$

where $C_{i,j}$ is the annual mean value of the i^{th} component in the j^{th} year. A positive component leads to an increase in the domain's heat content, and vice versa. $\sum_{i=1}^{i=n} |\text{RC}_{i,j}|$ is supposed to be 100%. Since $\text{RC}_{i,j}$ normally is not always positive or negative during a certain year, $\sum_{i=1}^{i=n} |\overline{\text{RC}}_{i,j}|$ is usually <100%.

The Student's t -test is used to estimate the statistical significance of the differences between climate experiments, as follows:

$$t = \frac{\overline{x^c} - \overline{x^a}}{s \sqrt{\frac{1}{n} + \frac{1}{m}}} \quad (10)$$

$$s^2 = \frac{\sum_1^n (x_i^c - \overline{x^c})^2 + \sum_1^m (x_i^a - \overline{x^a})^2}{n + m - 2} \quad (11)$$

where s is the unbiased estimator of sample variances; n and m are the sizes of these 2 samples; x_i^c and x_i^a are the sample variables, representing the annual means of 2 experiments in this study; and $\overline{x^c}$ and $\overline{x^a}$ are the corresponding sample means. In the presence of decadal variability, there are potential pitfalls with using a 36 yr historical period for reference

Table 1. Multi-annual mean \pm SD (Sv; 1 Sv = 10^6 m³ s⁻¹) of volume transports crossing open lateral boundaries (OLBs) under 3 scenarios. OLBs are indicated as red dots in Fig. 1. Positive transport is directed inward. **Bold**: significantly different from the 20C run at a 95 % confidence level. SBS: shelf break section; TAS: Taiwan Strait; TUS: Tsushima Strait

Fence name	20C (1970–2005)	RCP4.5 (2006–2099)	RCP8.5 (2006–2099)
SBS	0.79 \pm 0.28	0.80 \pm 0.33	0.96 \pm 0.39
TAS	1.42 \pm 0.12	1.46 \pm 0.15	1.41 \pm 0.17
TUS	-2.21 \pm 0.24	-2.25 \pm 0.27	-2.37 \pm 0.31
Net	0.00 \pm 0.02	0.01 \pm 0.02	0.01 \pm 0.02

while examining a nearly 100 yr scenario. Therefore, in this study, the linear trend is also calculated for each future scenario to strengthen the analysis.

3. RESULTS

3.1. Oceanic volume transport

The TAS and SBS are 2 main passages of water intrusion from the open ocean into the ECSs, while the TUS is an important export. Table 1 shows the annual mean net volume transport through the 3 OLBs under the 20C, RCP4.5 and RCP8.5 scenarios. In the 20C run, the annual mean volume transport is approximately 0.79, 1.42 and -2.21 Sv for the SBS, TAS and TUS, respectively. The strengths of the volume transports crossing these OLBs are consistent with the results of previous studies summarized in Zhou et al. (2015), indicating that the hydrodynamical model, as well as the method used to calculate the volume transport, is appropriate. The net volume transport of 0.00 ± 0.02 Sv crossing all 3 OLBs is reasonable, since the MPIOM model uses the Boussinesq and incompressibility approximations.

Relative to the 20C run, the annual mean net volume transports through the SBS and TUS both become larger under the RCP4.5 and RCP8.5 scenarios (Table 1). Regarding the TAS, the net volume transport shows a slight increase under the RCP4.5 scenario and a slight decrease under the RCP8.5 scenario when compared with the 20C run. Because the changes in volume transports through the OLBs nearly cancel each other out, the volume budget of the ECSs is nearly totally balanced by incoming and outgoing lateral fluxes for both RCP4.5 and RCP8.5 scenarios. Under these scenarios, the net volume lateral residual transports integrated over all OLBs amount to only 0.01 ± 0.02 Sv, averaged

over the entire projection period from 2006 to 2099. It can be assumed that this small residual is compensated for by the evaporation–precipitation balance and river input.

3.2. Heat budget

The OHC of the ECSs shows a rapid increase for recent decades and will continue to rise under the RCP4.5 and RCP8.5 scenarios (Fig. 2). The oceanic heat transport results in a net heat flow into the ECSs under the 20C, RCP4.5 and RCP8.5 scenarios, mostly balanced by the air–sea exchange, which shows a net heat loss from the ECSs (Fig. 2b). The quantita-

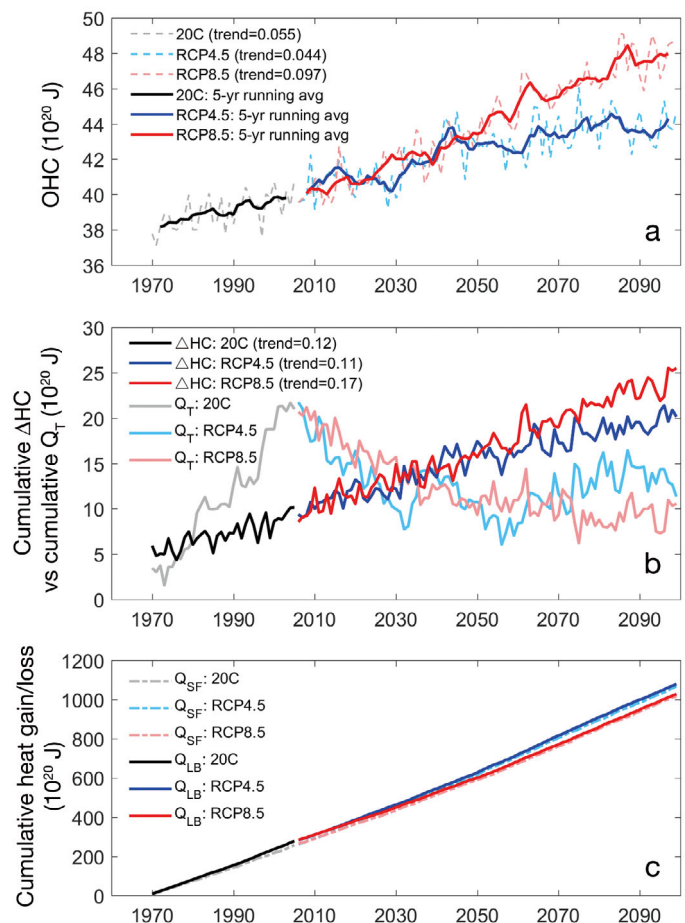


Fig. 2. (a) Time evolution of annual ocean heat content (OHC); (b) cumulative change in OHC (Δ HC, dark colors) and cumulative total net heat gain (Q_T , light colors, representing the sum of heat exchange through sea surface and lateral boundaries); (c) cumulative net heat gain or loss through the sea surface boundary (Q_{SF} , dashed lines, representing negative values, indicating that the ocean will lose heat) and through the lateral boundary (Q_{LB} , solid lines, representing positive values, indicating that the ocean will gain heat). Linear trends are significant at a 95 % confidence level for a 2-sided *F*-test

Table 2. Multi-annual mean \pm SD (10^{13} W) of heat gain or loss crossing open lateral boundaries (OLBs) and sea surface under 3 scenarios. OLBs are indicated as red dots in Fig. 1. Positive transport is directed inward. **Bold**: significantly different from the 20C run at a 95 % confidence level. Terms are defined in Section 2.3

Term	20C (1970–2005)	RCP4.5 (2006–2099)	RCP8.5 (2006–2099)
Q_{SBS}	-1.32 ± 0.45	-1.12 ± 0.64	-1.02 ± 0.67
Q_{TAS}	3.70 ± 0.31	3.75 ± 0.44	3.56 ± 0.46
Q_{TUS}	0.07 ± 0.26	0.09 ± 0.22	-0.01 ± 0.25
Q_S	12.34 ± 0.31	12.45 ± 0.36	12.38 ± 0.32
Q_L	-4.34 ± 0.15	-4.27 ± 0.18	-4.13 ± 0.19
Q_{LH}	-8.22 ± 0.39	-8.97 ± 0.49	-9.03 ± 0.61
Q_{SH}	-2.09 ± 0.20	-1.98 ± 0.21	-1.82 ± 0.24
Q_{LB}	2.45 ± 0.31	2.71 ± 0.44	2.54 ± 0.44
Q_{SF}	-2.30 ± 0.53	-2.77 ± 0.57	-2.61 ± 0.63
Q_T	0.15 ± 0.42	-0.06 ± 0.51	-0.07 ± 0.52

tive results for heat transport through the OLBs and sea surface are summarized in Table 2.

The total net heat gain (Q_T) caused by oceanic and air–sea heat exchanges is on the same order of magnitude as the change in the OHC (ΔHC). Note that the cumulative Q_T is approximately 10×10^{20} J larger

than the cumulative ΔHC by 2005, and approximately $(10 \times 10^{20} \text{ J}) - (15 \times 10^{20} \text{ J})$ smaller by the end of the 21st century (Fig. 2b). These small discrepancies are mostly due to the definition of reference temperature, for which there is no method of determination that is 100 % correct (Schauer & Beszczynska-Moller 2009). However, these differences are negligible when looking at the integrated heat fluxes, because they only account for approximately 4 and 1 % of the cumulative net heat exchange from the lateral or surface boundary, by 2005 and the end of the 21st century, respectively. Therefore, the REMO/MPIMO model as well as the method used to calculate the heat transport is appropriate.

3.3. Oceanic heat transport

3.3.1. Section-integrated and multi-annual mean

For the oceanic transport, the TAS is the major source of heat into the ECSs, while the SBS acts as the major sink (Table 2, Fig. 3). The strength of the net heat transport through the TAS is roughly 3 times

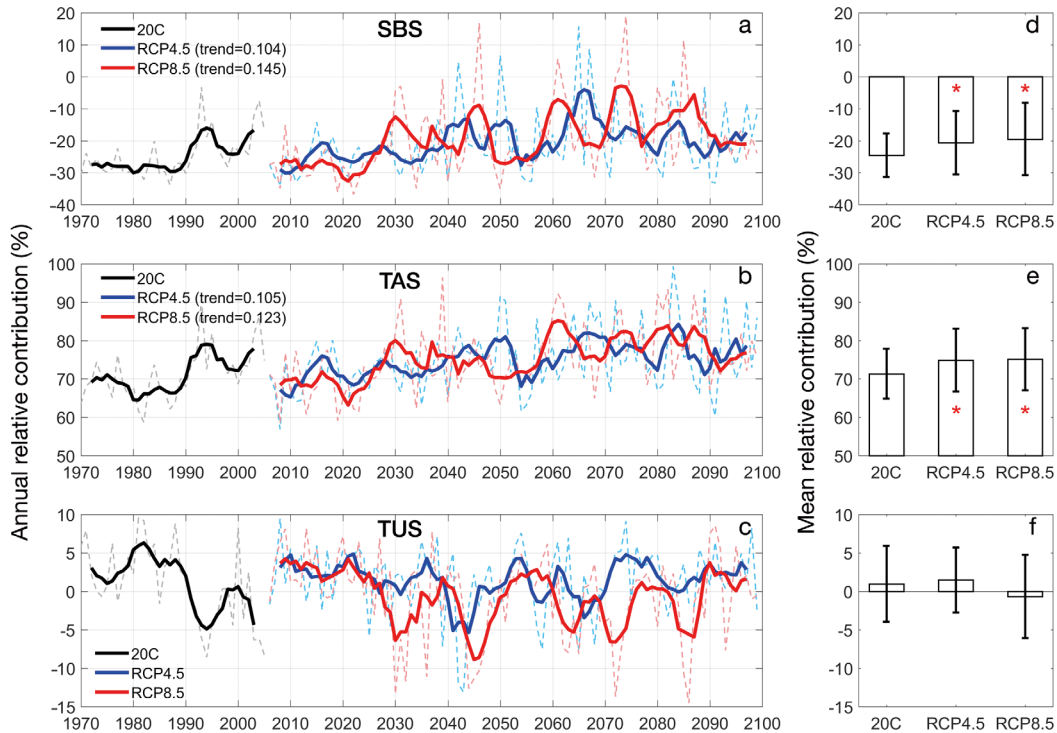


Fig. 3. (a–c) Annual relative contributions of 3 open lateral boundaries (OLBs) to the total lateral heat transport under the 20C (black), RCP4.5 (blue) and RCP8.5 (red) scenarios. Solid lines indicate 5 yr running averaged fields; dashed lines are annual mean values. (d–f) Mean relative contributions of 3 OLBs under 20C, RCP4.5 and RCP8.5 scenarios. Error bars represent ± 1 SD centered around the multi-annual mean. Linear trends are significant at a 95 % confidence level for a 2-sided F -test. Red star suggests the mean relative contribution under a future scenario (i.e. RCP4.5 and RCP8.5) is significantly different from the 20C run at a 95 % confidence level. SBS: shelf break section; TAS: Taiwan Strait; TUS: Tsushima Strait

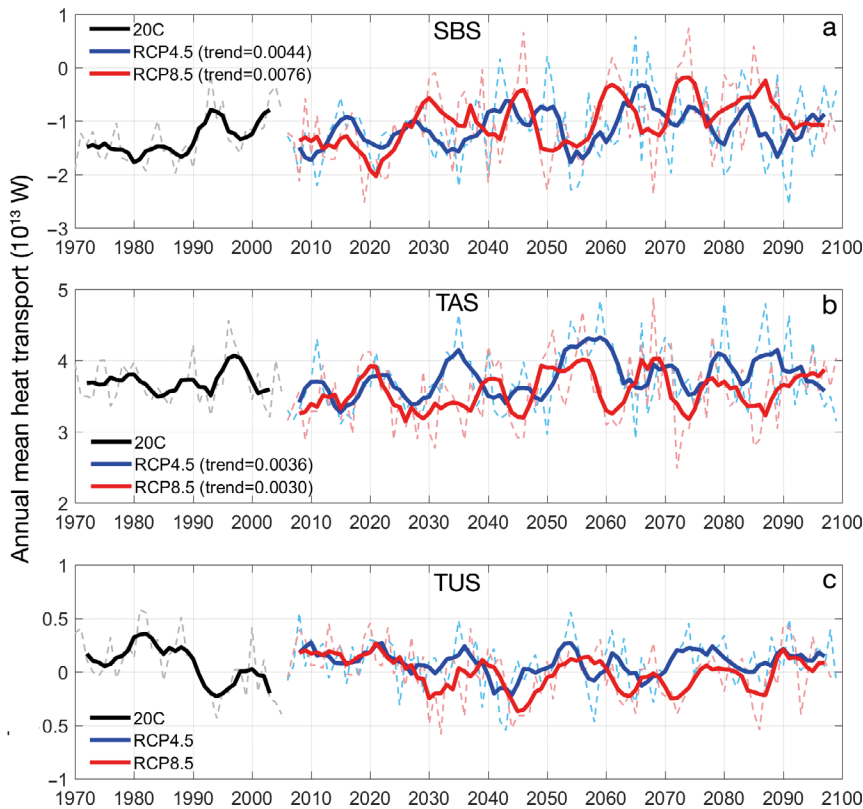


Fig. 4. (a–c) Annual mean heat transport through 3 open lateral boundaries (OLBs) under the 20C (black), RCP4.5 (blue) and RCP8.5 (red) scenarios. Solid lines indicate 5 yr running averaged fields; dashed lines are annual mean values. Only the linear trends for the shelf break section (SBS) under RCP8.5 and the Taiwan Strait (TAS) under RCP4.5 are significant at a 95 % confidence level for a 2-sided *F*-test. TUS: Tsushima Strait

that through the SBS, but in the opposite direction. In the 20C run, the TAS heat transport reaches a mean inward rate of 3.7×10^{13} W, mainly attributed to the TWC. Comparatively, the mean rate for the SBS is -1.32×10^{13} W in the 20C run. Despite a major water volume export of the ECSs, the net heat transport through the TUS is marginal and significantly smaller than the heat transport through the other 2 lateral boundaries.

Relative to the 20C run, the future change in the net heat transport through each boundary is consistent with the change in the corresponding net volume transport (Table 2). Specifically, the net heat transport (inward) through the TAS shows a slight increase under RCP4.5 compared with that under 20C, and a slight decrease occurs under RCP8.5. Regarding the SBS, the net heat transport (outward) declines slightly under RCP4.5 and RCP8.5, compared with the value under 20C. In contrast, the net heat transport (inward) through the TUS would increase slightly under RCP4.5 compared with that under

20C, while it turns to a net outward heat transport under RCP8.5. Consequently, the total net heat transport into the ECSs through the OLBs is largest for the RCP4.5 scenario and not for the RCP8.5 scenario.

The yearly relative contributions to the corresponding total lateral heat transport for the SBS, TAS and TUS are presented in Fig. 3. In the 20C run, the mean relative contributions of the TAS, SBS and TUS are 71.3 ± 6.5 , -24.5 ± 6.7 and 1.0 ± 5.0 %, respectively. Consistent with the TAS net heat transport, the relative contribution of the TAS also shows a moderate increasing trend under both RCP4.5 and RCP8.5, except for the obvious decadal variability. The relative contribution of the SBS as well as the SBS net heat transport shows a moderate declining trend under these scenarios (Figs. 3 & 4). Averaged over the whole period for the RCP scenarios, the mean relative contributions of the TAS, SBS and TUS are 74.9 ± 8.2 % (75.2 ± 8.1 %), -20.7 ± 9.9 % (-19.5 ± 11.3 %) and 1.5 ± 4.2 % (-0.7 ± 5.4 %), respectively, under the RCP4.5 (RCP8.5) scenario.

3.3.2. Spatial and temporal variation

Because of the warm water carried by the Kuroshio Current and the TWC, an inward (outward) volume transport across the SBS and TAS leads to an inward (outward) heat transport (Fig. 5a). For the SBS, volume and heat exchanges exhibit large variabilities among different locations along this boundary. Generally, they are more pronounced in the southern part of the SBS compared to the northern part. The net heat transport is inward in the surface and bottom layers but outward in the mid-water layer (Fig. 6), suggesting a 3-layer structure which is consistent with the finding of J. Zhang et al. (2017).

For TAS, a more pronounced volume and heat inflow occurs near Taiwan island (locations 9 and 10), where the bathymetry is deeper than in the other regions (Fig. 5b). The transports across the TAS are mostly pointing in the same direction and are vertically nearly homogeneous (figure not shown). The

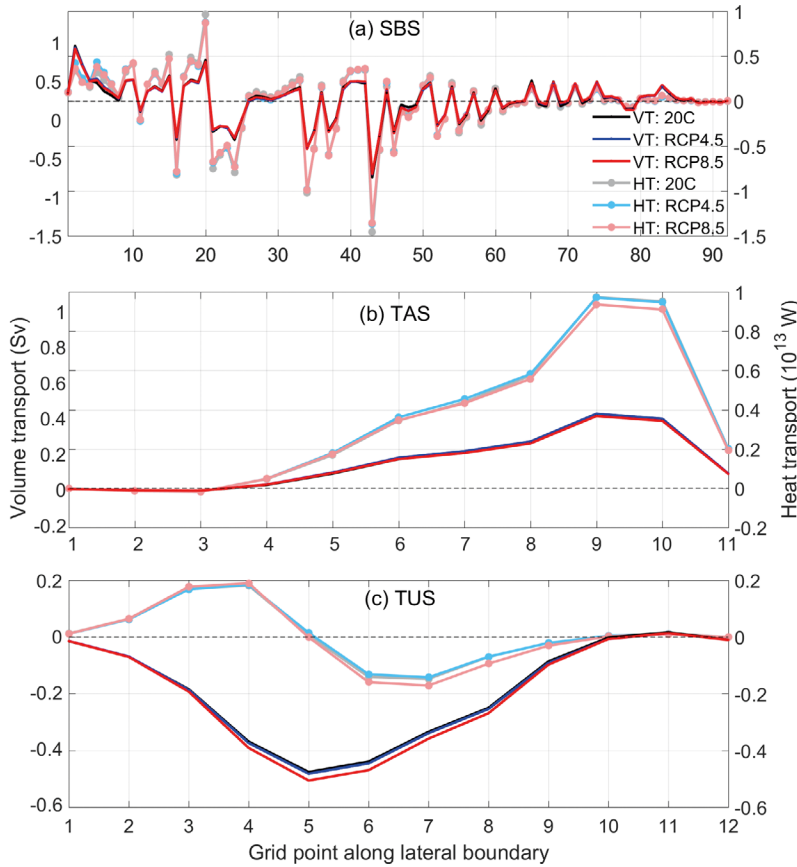


Fig. 5. Multi-annual mean volume transport (VT) (dark-colored lines; left y-axis) and heat transport (HT) (light-colored lines; right y-axis) across the (a) shelf break section (SBS), (b) Taiwan Strait (TAS) and (c) Tsushima Strait (TUS) under the 20C (black), RCP4.5 (blue) and RCP8.5 (red) scenarios. The x-axis represents grid points along these sections, running from west to east (see Fig. 1)

net heat transport in each layer is inward, and the upper-layer water brings a larger amount of heat into the ECSs (Fig. 7). Roughly estimated, the water body of the upper 25 m accounts for 50 % of the entire heat transport through the TAS into the ECSs under RCP4.5 and RCP8.5.

The volume transport across the TUS is outward at almost all locations, with a maximum outflow at location 5 (Fig. 5c). Different from the volume transport, the heat transport across the TUS has 2 extremes, with maximum inward transport at locations 3 and 4 and maximum outward transport at locations 6 and 7. Such a situation can easily occur when temperatures are close to the reference temperature. The net heat transport is usually outward at depths of <70 m and inward at depths of >70 m (Fig. 8).

The heat transport through the OLBs exhibits a significant interannual to decadal variability (Figs. 6–8). This variability is probably affected by phenomena

such as the ENSO and PDO (Hwang & Kao 2002, Hsin et al. 2013, Wu 2013, Wu et al. 2014). However, the investigation of these linkages is not the focus of the current study.

3.4. Air–sea heat exchange

3.4.1. Regional average

The annual mean net heat loss from the ECSs into the atmosphere is around 2.30×10^{13} W (about 28.3 W m^{-2}) averaged in the 20C run and is projected to increase under the RCP4.5 and RCP8.5 scenarios (Table 2).

The multi-annual mean results show that, overall, the ECSs absorb radiative heat from solar radiation and release heat to the atmosphere through longwave radiation, evaporation and sensible heat exchange (Table 2). Among these, evaporation is the most important mechanism for sea surface heat loss. Relative to the 20C run, except for the net shortwave radiation, the future changes in the other 3 components are significant at a 95 % confidence level. Specifically, the latent heat flux shows a marked increase under the RCP4.5 and RCP8.5 scenarios, while the heat loss through longwave radiation and sensible heat flux shows a marked reduction (Table 3).

The yearly relative contributions to the corresponding total sea surface heat transport for these 4 components are presented in Fig. 9, indicating that the net shortwave radiation provides a positive contribution to the surface heat budget, while the others represent negative contributions. Apparently, the proportion is the largest for the net shortwave radiation, followed by the latent heat flux and the net longwave radiation, and is the least for the sensible heat flux under each scenario. In the 20C run, the mean relative contributions of shortwave radiation, latent heat flux, longwave radiation and sensible heat flux averaged over the period of 1970–2005 amount to approximately 45.6 ± 0.9 , -30.4 ± 0.8 , -16.1 ± 0.4 and -7.8 ± 0.6 %, respectively.

The future change in the relative contribution of each component is significant when compared with

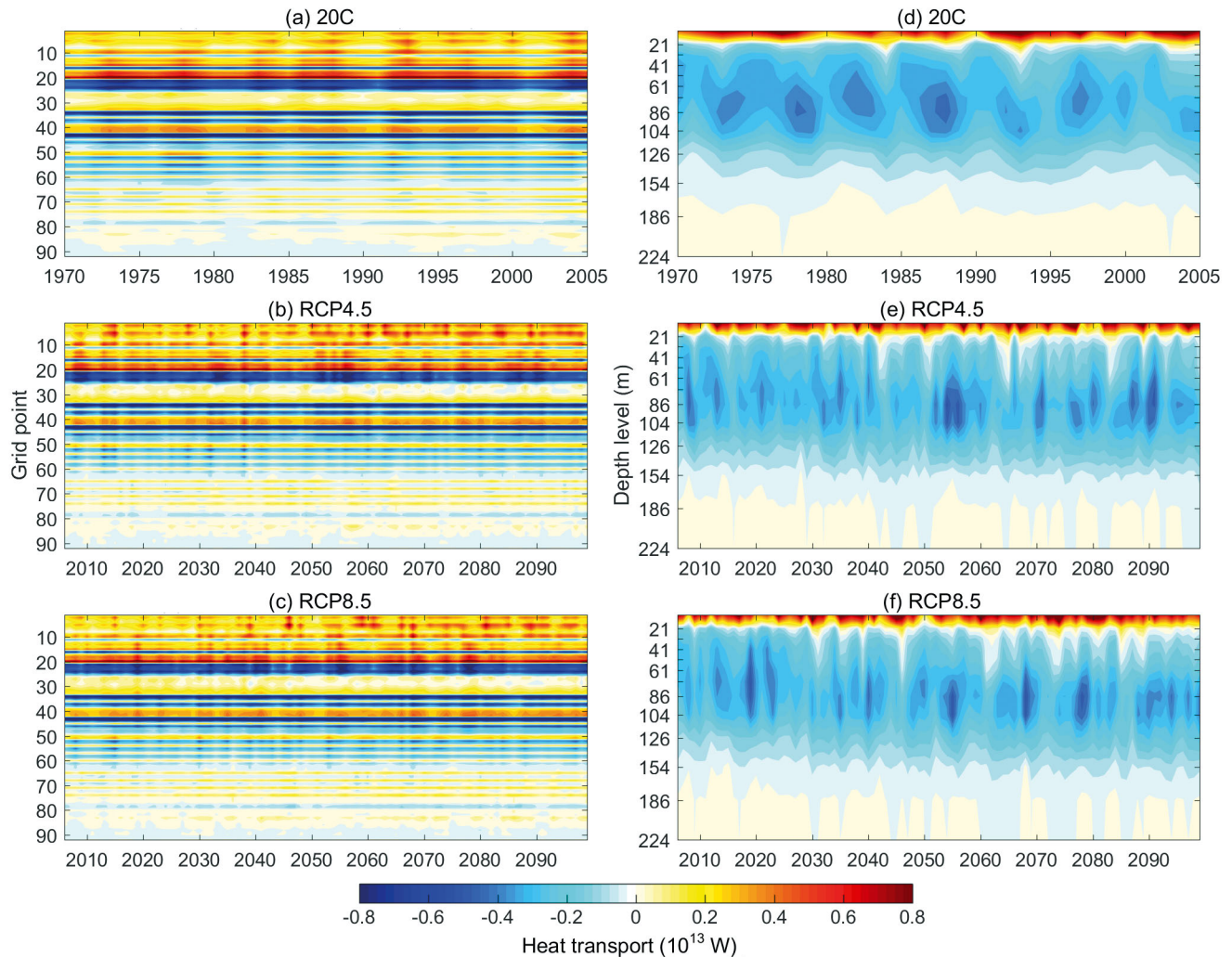


Fig. 6. Annual mean heat transport across the shelf break section under the (a,d) 20C, (b,e) RCP4.5 and (c,f) RCP8.5 scenarios. The uppermost portion of the y-axis represents the westernmost position on these sections (see Fig. 1). Warm/cool colors indicate heat transport into/out of the eastern China seas

the 20C run (Fig. 9). Specifically, the relative contribution for latent heat flux shows an obvious increasing trend, and the relative contributions for thermal radiation and sensible heat flux present a markedly declining trend under RCP4.5 and RCP8.5. Averaged over the whole period for the RCP scenarios, the mean relative contributions are $45.0 \pm 0.9\%$ ($45.3 \pm 1.0\%$), $-15.4 \pm 0.4\%$ ($-15.1 \pm 0.6\%$), $-32.4 \pm 1.0\%$ ($-33.0 \pm 1.5\%$) and $-7.1 \pm 0.6\%$ ($-6.7 \pm 0.8\%$) for the shortwave radiation, longwave radiation latent heat flux and sensible heat flux, respectively, under scenario RCP4.5 (RCP8.5). Notably, among these air–sea flux terms, the relative contribution of the latent heat flux shows largest changes compared to the 20C run for both RCP4.5 and RCP8.5 scenarios, suggesting that the increased heat loss from the sea surface under each RCP scenario is mainly a consequence of the strengthened evaporation over the ECSs.

3.4.2. Spatial distribution

Except for regions with bathymetry shallower than approximately 50 m, nearly the entire ECSs will lose heat through the air–sea exchange (Fig. 10a). The shallow ocean exhibits a smaller heat loss compared with the deeper ocean, indicating a close relationship between the surface heat flux and topography of the ECSs. The future change in the net heat flux shows a similar spatial variation also for the future scenarios RCP4.5 and RCP8.5, i.e. the heat loss through the air–sea exchange increases over most of the ECSs, with the maximum increase occurring at the northern Taiwan coast (Fig. 10b,c). As a joint consequence of the surface radiative and nonradiative components, the spatial features of the surface net heat flux are mostly dominated by the spatial patterns in latent heat flux. This is consistent across hindcast scenario

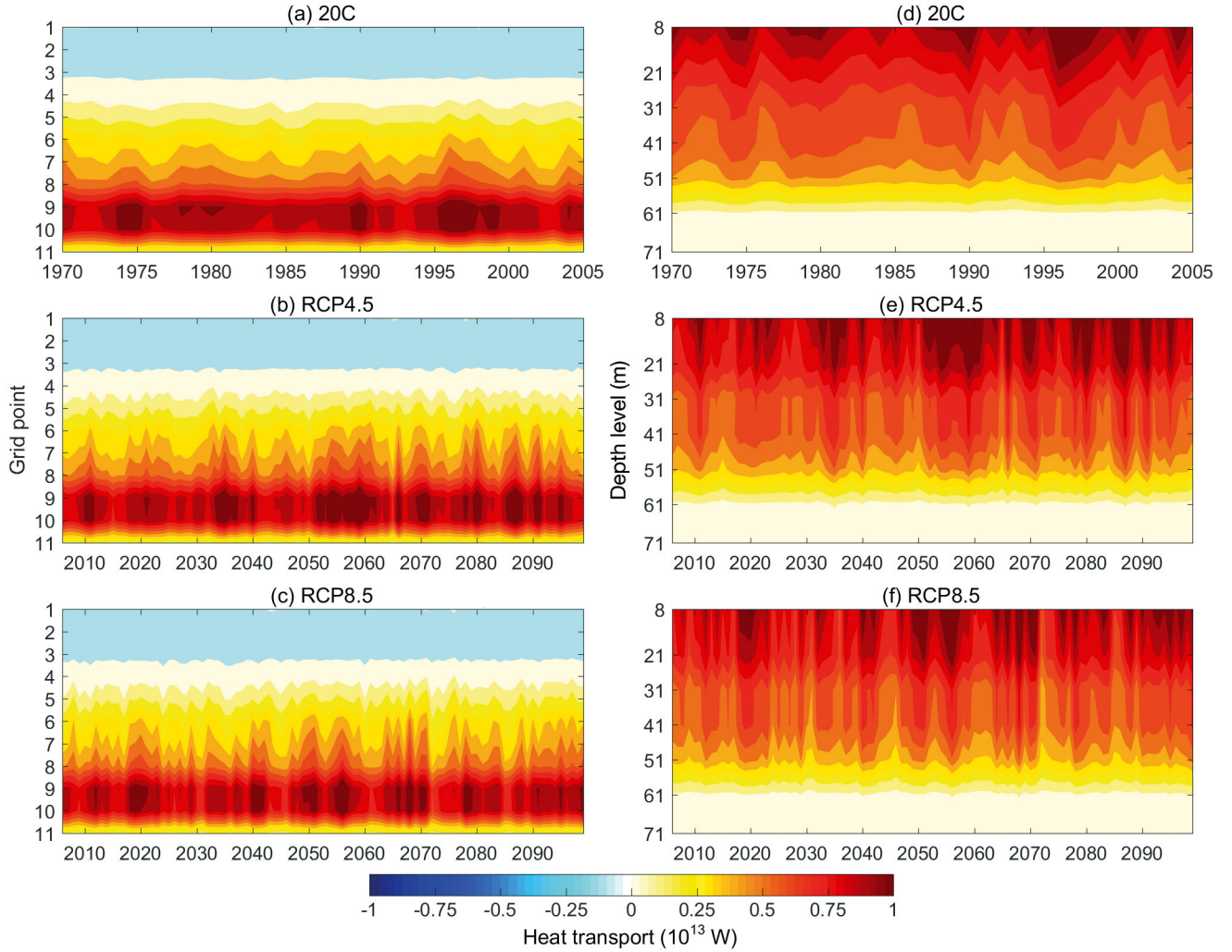


Fig. 7. Annual mean heat transport across the Taiwan Strait under the (a,d) 20C, (b,e) RCP4.5 and (c,f) RCP8.5 scenarios. The uppermost portion of the y-axis represents the westernmost position on these sections (see Fig. 1). Warm/cool colors indicate heat transport into/out of the eastern China seas

20C as well as the 2 forecast scenarios, RCP4.5 and RCP8.5 (Fig. 11).

The spatial changes in shortwave radiation, longwave radiation, latent heat flux and sensible heat flux under RCP4.5 and RCP8.5 are shown in Fig. 11. The future response of the latent heat flux is the largest among these 4 components, with a maximum appearing near the northern Taiwan coast which is mainly attributed to the changes in surface wind and SST. The increases in the surface wind speed and SST could accelerate surface evaporation and enhance the upward latent heat flux (Fig. 12). Cloud cover plays a key role in the distribution of shortwave radiation (Fig. 13). Less cloud cover leads to more solar radiation being absorbed by seawater due to a weaker shortwave cloud radiative effect (CRE). The distribution of longwave radiation is also affected by the adjustment of cloud cover; that is, less cloud cover reduces down-

ward longwave radiation due to a weaker longwave CRE (Fig. 13). The sensible heat flux shows a close correlation with the SST distribution. The SST increase strengthens the upward sensible heat flux. Because of a more pronounced warming of the atmospheric SST compared to the SST, the heat flux from the ECSs into the atmosphere by thermal radiation and sensible heat flux will be reduced under both projection scenarios.

4. DISCUSSION

This study demonstrates that the SBS constitutes the major heat export pathway of the ECSs, whereas the net heat transport through the TUS is marginal. These results are inconsistent with some previous studies (Liu et al. 2010, Zhou et al. 2015), which concluded that the SBS is an important heat source of

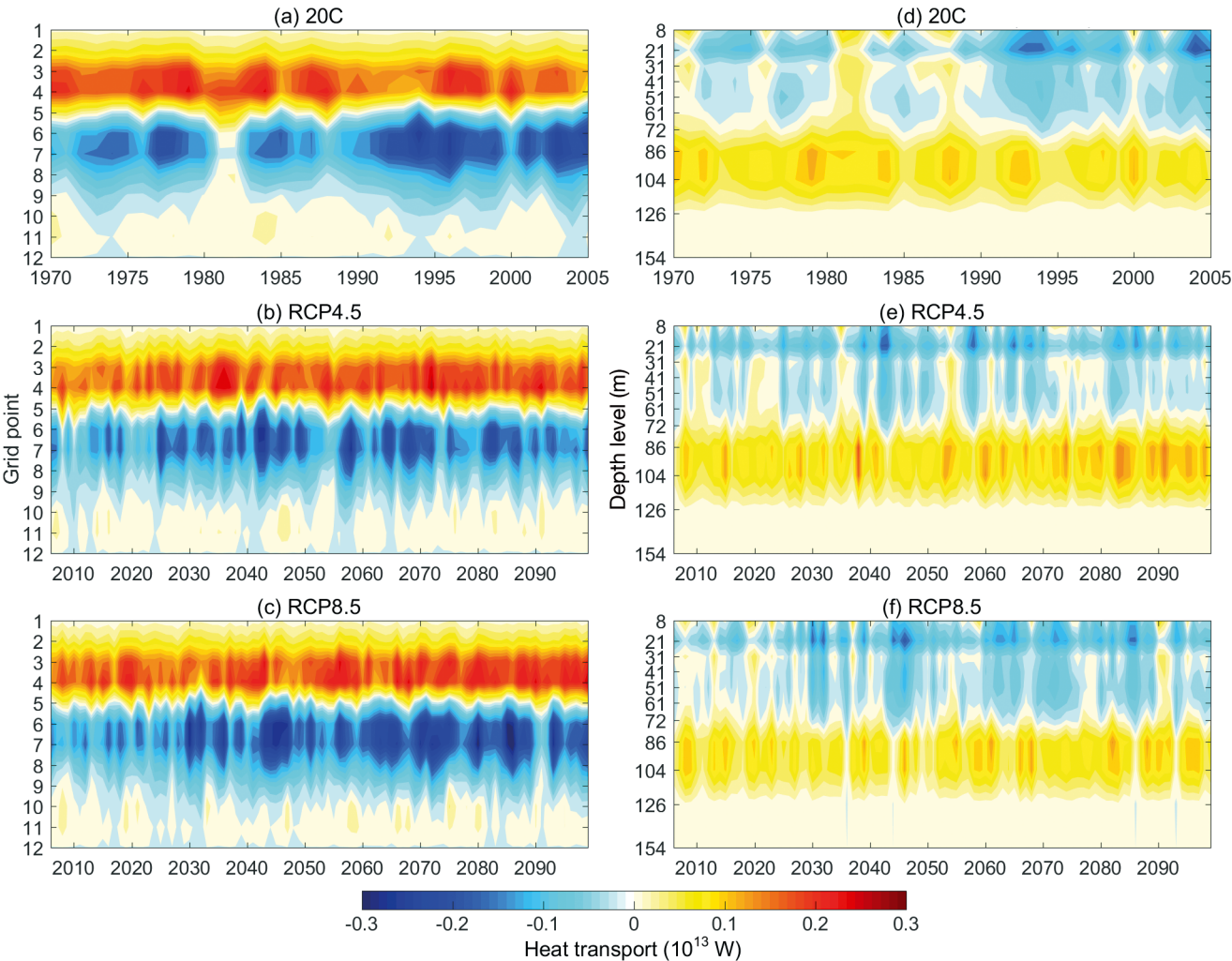


Fig. 8. Annual mean heat transport across the Tsushima Strait under the (a,d) 20C, (b,e) RCP4.5 and (c,f) RCP8.5 scenarios. The uppermost portion of the y-axis represents the westernmost position on these sections (see Fig. 1). Warm/cool colors indicate heat transport into/out of the eastern China seas

Table 3. Linear trends in surface heat fluxes under RCP scenarios ($\text{W m}^{-2} \text{ yr}^{-1}$). Positive transport is directed inward. **Bold**: significant at the 5% significance level for a 2-sided F -test

Component	RCP4.5 (2006–2099)	RCP8.5 (2006–2099)
Shortwave radiation	0.018	0.003
Longwave radiation	0.022	0.045
Latent heat flux	−0.100	−0.191
Sensible heat flux	0.016	0.054

ECSs, while the TUS is an important export pathway. This discordance is mainly related to the methods employed to calculate the lateral heat transport, as mentioned in Section 2. As stated by Schauer & Beszczynska-Moller (2009), one should be careful about the choice of temperature scale when calculat-

ing oceanic heat transport. In this study, oceanic heat transport is defined as the flux of the temperature anomaly relative to a reference temperature, which according to Schauer & Beszczynska-Moller (2009) gives more realistic results compared to the standard method, where the heat flux is calculated relative to 0.0°C or 0.0 K. The spatial distribution of sea temperature thus becomes a key factor to impact the direction of heat transport as well as its amount. Note the introduction of the additional varying factor, i.e. ΔT , may result in a larger temporal variability in heat transport than the corresponding volume transport (Tables 1 & 2). In contrast, the net annual mean heat transport through all OLBs amounts to around $2.45 \times 10^{13} \text{ W}$ in the 20C run, which is of the same order of magnitude as the results of Zhou et al. (2015) and Liu et al. (2010), i.e. $5.0 \times 10^{13} \text{ W}$ for the year 2006 and $4.0 \times 10^{13} \text{ W}$ for the years 1995–1999, respectively.

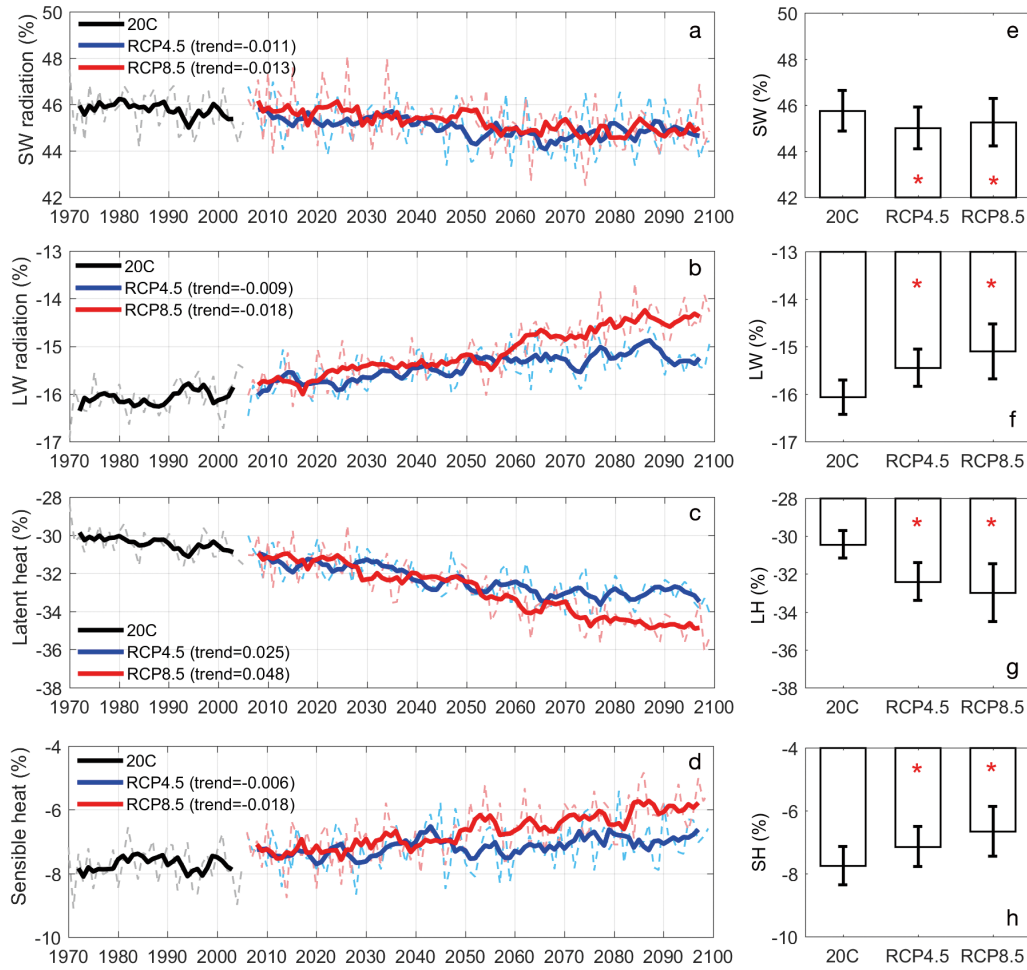


Fig. 9. (a–d) Annual relative contributions of 4 major components of total surface heat flux into the eastern China seas under the 20C (black), RCP4.5 (blue) and RCP8.5 (red) scenarios. Solid lines indicate 5 yr running averaged fields; dashed lines are annual mean values. (e–h) Mean relative contributions of 4 components under 20C, RCP4.5 and RCP8.5 scenarios. Linear trends are significant at a 95 % confidence level for a 2-sided F -test. Error bars represent ± 1 SD centered around the multi-annual mean. Red star suggests the mean relative contribution under the future scenario (i.e. RCP4.5 and RCP8.5) is significantly different from the 20C run at a 95 % confidence level. SW: shortwave; LW: longwave; LH: latent heat; SH: sensible heat

The net lateral heat transport is projected to increase under the RCP4.5 and RCP8.5 scenarios, mainly attributed to the decrease in the net outward heat transport through the SBS. The reduced outflow of heat through the SBS is due to a stronger inward volume flux through the SBS. Interestingly, the total net heat transport into the ECSs through the OLBs is largest for the RCP4.5 scenario and not for the RCP8.5 scenario. Such a difference in net heat transport between RCP4.5 and RCP8.5 is mainly associated with future changes in the TAS volume transport. This study suggests that the volume transport through major straits of the ECSs, except for the TAS, is projected to increase slightly under the RCP scenarios, which matches well with the previous re-

search based on the SRES A1B scenario (Seo et al. 2014). The northeasterly wind stress in the ECS shows a more obvious change under RCP8.5 than that under RCP4.5 (Fig. 12), which may impact the volume transports. The northeasterly wind stress changes may induce an onshore flow anomaly through the SBS and an outward flow anomaly through the TUS. Meanwhile, the flow through the TAS into the ECS may be blocked by the onshore flow anomaly in the ECS. This possible mechanism for future volume transport changes has also been identified by Seo et al. (2014).

The climatology of surface net heat flux shows that a larger upward heat flux occurs for the deeper parts of the ocean than for the shallow waters of the ECSs

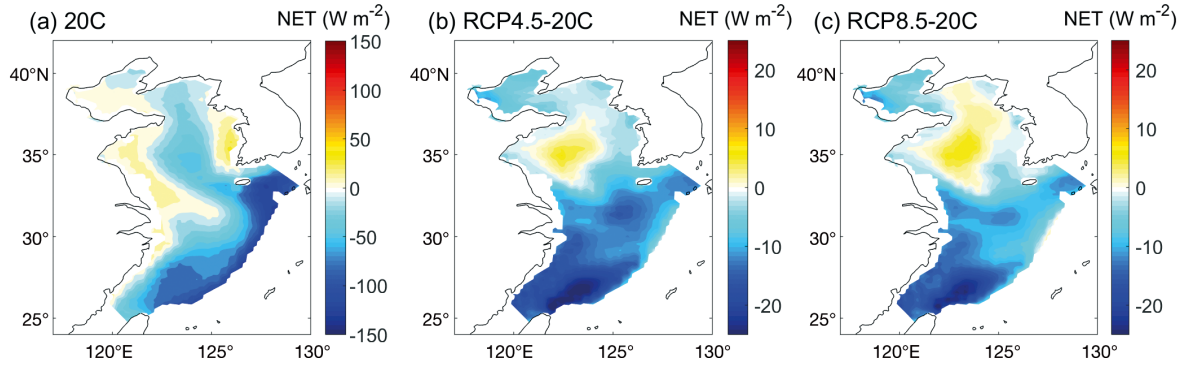


Fig. 10. Net heat flux (NET) over the eastern China seas. (a) Climatological average over the period 1970–2005. (b,c) Changes at the end of the 21st century (2064–2099), relative to 1970–2005, under the (b) RCP4.5 and (c) RCP8.5 scenarios. Warm/cool colors indicate net heat flux into/out of the ECSs

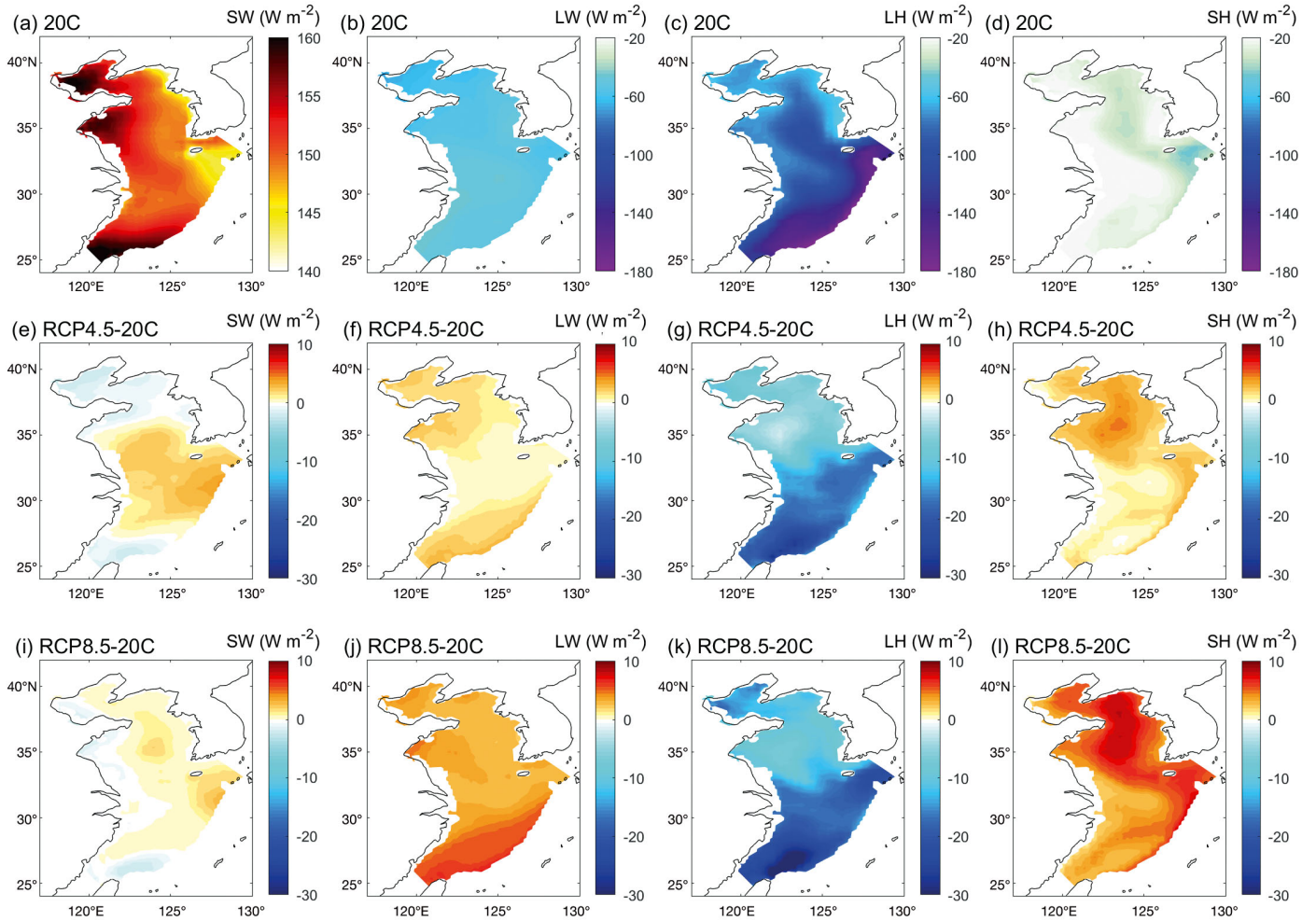


Fig. 11. Sea surface heat flux over the eastern China seas (ECSs). (a–d) Climatological average over the period 1970–2005. (e–l) Changes at the end of the 21st century (2064–2099), relative to 1970–2005, under the (e–h) RCP4.5 and (i–l) RCP8.5 scenarios. From left to right: shortwave radiation SW, longwave radiation LW, latent heat flux LH, and sensible heat flux SH. Warm/cool colors indicate heat flux into/out of the ECSs

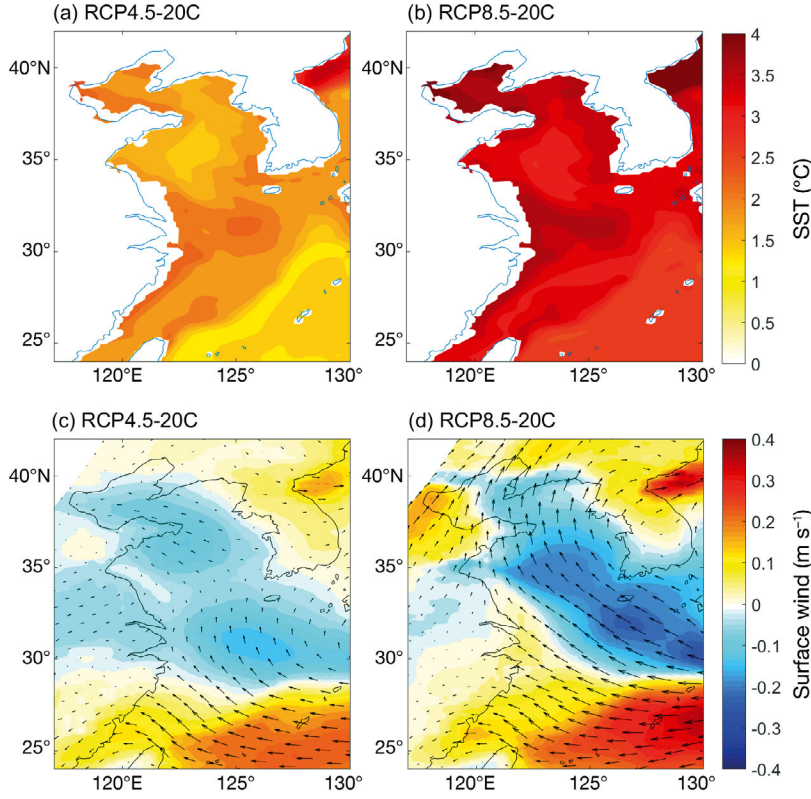


Fig. 12. Changes at the end of the 21st century (2064–2099) under the RCP4.5 and RCP8.5 scenarios, relative to 1970–2005. (a,b) Sea surface temperature; (c,d) surface wind speed

(Fig. 10a), implying a close correlation between the surface heat flux and the bottom topography, which is in agreement with the findings of Xie et al. (2002). That is, there is a linear relationship between the thermal inertia of a shelf water column and bottom depth; the ECSs water is well mixed up to 100 m depth under the intense winter cooling. This indicates that the heat capacity over the entire winter period depends mostly linearly on the water depth. In particular, shallow areas, cool much faster than deep areas, and also stay colder in winter. As the ocean–

atmosphere heat flux is strongly dependent on SST, the upward heat flux over the shallow water in turn is reduced due to the colder surface temperature.

In this study, the estimated heat balance in the ECSs cannot be closed (Fig. 2, Table 2). Since the changes in the heat content are given by the residual of the much larger incoming and outgoing heat fluxes, small errors in the heat fluxes can result in large errors in the heat content changes. There are 2 major sources where the errors in these fluxes may occur.

(1) The definition of the reference temperature, which (as stated in Section 2.3), in this study is defined as the domain's average temperature of each layer. As an example, Q_{LB} is 2.45×10^{13} W and Q_T is 0.15×10^{13} W, averaged over the 20C run (Table 2). If, instead, the reference temperature would be defined as the domain volume average temperature, Q_{LB} will become 1.74×10^{13} W and Q_T will become -0.56×10^{13} W, averaged over the 20C run. However, with the latter definition, the

discrepancies between the cumulative Q_T and the OHC change also will get larger, which indicates that our current definition is more appropriate.

(2) The discrepancies in the heat balance may be caused by the neglect of submonthly variations, when calculating the heat fluxes by multiplying monthly mean transport rates with monthly mean temperature values. Obviously, the nonlinearity between these 2 parameters on submonthly time scales is not accounted for when using the available monthly model output data.

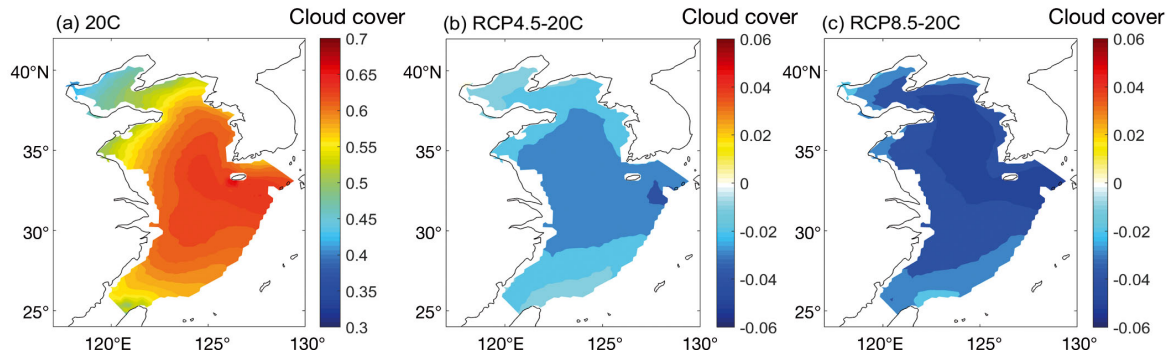


Fig. 13. Cloud cover over the eastern China seas. (a) Climatological average over the period 1970–2005. (b,c) Changes at the end of the 21st century (2064–2099), relative to 1970–2005, under the (b) RCP4.5 and (c) RCP8.5 scenarios

However, these discrepancies in the heat balance do not impact our general conclusions. The heat fluxes, which are the focus of the current study, are at least 1 order of magnitude larger than the residual of the incoming and outgoing fluxes, which causes the heat balance inconsistencies.

Another uncertainty of our approach is that the results of this study are solely based on 1 single coupled system model. The multi-model ensemble projection is a popular method to reduce this uncertainty, but requires extensive computer resources. To further validate our results, another 3 simulations using different forcing and a different model setting were used (see the Supplement). It is suggested from this exercise that in the frame of the current study, a multi-member ensemble approach would not be essential to improve the reliability of our results. This is in line with our finding that both the spatial distribution and the integrated value of the lateral volume and heat transport determined in this study are mostly in accordance with previous studies. The main characteristic of the spatial change in SST (Fig. 12) is also consistent with Yu et al. (2012), who demonstrated that the temperatures in the coastal ocean will potentially show a stronger increase than those in the open ocean under the background of global warming. Taking the latter into account, it can be expected that the newly derived heat flux changes given in the present study also provide realistic estimates.

5. CONCLUSIONS

This study provides a reasonable projection of the impacts of global change on the ECSs and, moreover, deepens our understanding of the major processes which control the ocean temperature changes in these seas.

Solar radiation contributes the largest heat source of the ECSs. The heat gain achieved by solar radiation is cancelled out by thermal radiation, latent heat flux and sensible heat flux released at the ocean surface. The air–sea heat exchange thus cools the ECSs, whereas an overall warming is found for the ECSs. An increased oceanic heat transport by ocean currents balances this reduced heat supply by the sea surface heat fluxes. In particular, water transport through the TAS brings the largest amount of heat into the ECSs. Despite an inward heat transport onto the ECS shelf caused by the Kuroshio intrusion occurring northeast of Taiwan, overall, the SBS acts as a heat sink for the ECSs. The net heat gain or loss by the TUS is marginal.

Under the climate projection scenarios, the net heat loss from the SBS decreases, probably associated with the change in surface wind. Thus, the net heat transported into the ECSs through the lateral boundaries increases slightly under these scenarios, leading to an overall warming of the ECSs, relative to the 20C run. Notably, the warmer SST, along with strengthened wind, further enhances the surface evaporation, providing a negative feedback onto the net effect of oceanic transport.

Acknowledgements. This work was jointly supported by the National Key Research & Development Plan of China (No. 2016YFC1401603); a grant from the Scientific Research Fund of the Second Institute of Oceanography, SOA (No. JG1620); the National Natural Science Foundation of China (Nos. 41705048 and 41621064); the Zhejiang Provincial Natural Science Foundation of China (No. LR16D060001); Sino-German cooperation in ocean and polar research; the state assignment of FASO Russia (theme 0149-2019-0015); and the Joint Advanced Marine and Ecological Studies in the Bay of Bengal and the eastern equatorial Indian Ocean (JAMES). We thank the anonymous reviewers for their useful comments and suggestions. To access the model output used in this paper, please contact Jian Su at jis@dmu.dk.

LITERATURE CITED

- ✦ Belkin IM (2009) Rapid warming of large marine ecosystems. *Prog Oceanogr* 81:207–213
- ✦ Breitbart D, Levin LA, Oschlies A, Grégoire M and others (2018) Declining oxygen in the global ocean and coastal waters. *Science* 359:eaam7240
- ✦ Cheng L, Trenberth KE, Fasullo J, Boyer T, Abraham J, Zhu J (2017) Improved estimates of ocean heat content from 1960 to 2015. *Sci Adv* 3:e1601545
- ✦ Chern CS, Wang J, Wang DP (1990) The exchange of Kuroshio and East China Sea shelf water. *J Geophys Res* 95: 16017–16023
- ✦ Domingues CM, Church JA, White NJ, Gleckler PJ, Wijffels SE, Barker PM, Dunn JR (2008) Improved estimates of upper-ocean warming and multi-decadal sea-level rise. *Nature* 453:1090–1093
- ✦ ESR (Earth Space Research) (2009) OSCAR third degree resolution ocean surface currents, Ver 1. PO.DAAC, Pasadena, CA. <http://dx.doi.org/10.5067/OSCAR-03D01> (accessed 10 Aug 2018)
- ✦ Gilbert D, Rabalais NN, Díaz RJ, Zhang J (2010) Evidence for greater oxygen decline rates in the coastal ocean than in the open ocean. *Biogeosciences* 7:2283–2296
- ✦ Giorgetta MA, Jungclaus J, Reick CH, Legutke S and others (2013) Climate and carbon cycle changes from 1850 to 2100 in MPI-ESM simulations for the Coupled Model Intercomparison Project phase 5. *J Adv Model Earth Syst* 5:572–597
- ✦ Guo X, Miyazawa Y, Yamagata T (2006) The Kuroshio on-shore intrusion along the shelf break of the East China Sea: the origin of the Tsushima Warm Current. *J Phys Oceanogr* 36:2205–2231
- ✦ Harley CD, Randall Hughes A, Hultgren KM, Miner BG and others (2006) The impacts of climate change in coastal marine systems. *Ecol Lett* 9:228–241

- ✦ Hsin YC, Qiu B, Chiang TL, Wu CR (2013) Seasonal to inter-annual variations in the intensity and central position of the surface Kuroshio east of Taiwan. *J Geophys Res Oceans* 118:4305–4316
- Huang D, Ni X, Tang Q, Zhu X, Xu D (2012) Spatial and temporal variability of sea surface temperature in the Yellow Sea and East China Sea over the past 141 years. In: Wang SY (ed) *Modern climatology*. InTech, Rijeka, p 213–234
- ✦ Huang D, Zeng D, Ni X, Zhang T and others (2016) Along-shore and cross-shore circulations and their response to winter monsoon in the western East China Sea. *Deep Sea Res II* 124:6–18
- ✦ Hwang C, Kao R (2002) TOPEX/POSEIDON-derived space-time variations of the Kuroshio Current: applications of a gravimetric geoid and wavelet analysis. *Geophys J Int* 151:835–847
- ✦ Ichikawa H, Beardsley RC (2002) The current system in the Yellow and East China seas. *J Oceanogr* 58:77–92
- IPCC (2013) *Climate change 2013: the physical science basis*. In: Stocker TF, Qin D, Plattner GK, Tignor M and others (eds) *Contribution of Working Group I to the Fifth Assessment Report of the Intergovernmental Panel on Climate Change*. Cambridge University Press, Cambridge
- ✦ Isobe A (1999) The Taiwan-Tsushima Warm Current System: its path and the transformation of the water mass in the East China Sea. *J Oceanogr* 55:185–195
- ✦ Isobe A (2008) Recent advances in ocean-circulation research on the Yellow Sea and East China Sea shelves. *J Oceanogr* 64:569–584
- ✦ Isobe A, Beardsley RC (2006) An estimate of the cross-frontal transport at the shelf break of the East China Sea with the Finite Volume Coastal Ocean Model. *J Geophys Res* 111:C03012
- ✦ Jacob D, Podzun R (1997) Sensitivity studies with the regional climate model REMO. *Meteorol Atmos Phys* 63: 119–129
- ✦ Jacob D, Elizalde A, Haensler A, Hagemann S and others (2012) Assessing the transferability of the Regional Climate Model REMO to different Coordinated Regional Climate Downscaling Experiment (CORDEX) regions. *Atmosphere* 3:181–199
- ✦ Jung HK, Rahman SMM, Kang CK, Park SY and others (2017) The influence of climate regime shifts on the marine environment and ecosystems in the East Asian marginal seas and their mechanisms. *Deep Sea Res II* 143:110–120
- ✦ Jungclauss JH, Fischer N, Haak H, Lohmann K and others (2013) Characteristics of the ocean simulations in the Max Planck Institute Ocean Model (MPIOM) the ocean component of the MPI-Earth system model. *J Adv Model Earth Syst* 5:422–446
- ✦ Keeling RE, Kortzinger A, Gruber N (2010) Ocean deoxygenation in a warming world. *Annu Rev Mar Sci* 2: 199–229
- ✦ Kim SB, Lee T, Fukumori I (2004) The 1997–1999 abrupt change of the upper ocean temperature in the north central Pacific. *Geophys Res Lett* 31:L22304
- ✦ Kim YS, Jang CJ, Yehc SW (2018) Recent surface cooling in the Yellow and East China seas and the associated North Pacific climate regime shift. *Cont Shelf Res* 156:43–54
- ✦ Lee JS, Takeshi M (2007) Intrusion of Kuroshio water onto the continental shelf of the East China Sea. *J Oceanogr* 63:309–325
- ✦ Lee T, Fukumori I, Tang B (2004) Temperature advection: internal versus external processes. *J Phys Oceanogr* 34: 1936–1944
- ✦ Levitus S, Antonov JI, Boyer TP, Stephens C (2000) Warming of the world ocean. *Science* 287:2225–2229
- ✦ Levitus S, Antonov JI, Boyer TP, Baranova OK and others (2012) World ocean heat content and thermosteric sea level change (0–2000 m), 1955–2010. *Geophys Res Lett* 39:L10603
- ✦ Li R, Jing Z, Chen Z, Wu L (2017) Response of the Kuroshio Extension path state to near-term global warming in CMIP5 experiments with MIROC4h. *J Geophys Res Oceans* 122:2871–2883
- ✦ Lima FP, Wetthey DS (2012) Three decades of high-resolution coastal sea surface temperatures reveal more than warming. *Nat Commun* 3:1–13
- ✦ Lin C, Su J, Xu B, Tang Q (2001) Long-term variations of temperature and salinity of the Bohai Sea and their influence on its ecosystem. *Prog Oceanogr* 49:7–19
- ✦ Lin C, Ning X, Su J, Lin Y, Xu B (2005) Environmental changes and the responses of the ecosystems of the Yellow Sea during 1976–2000. *J Mar Syst* 55:223–234
- ✦ Liu C, Wang F, Chen X, von Storch JS (2014) Interannual variability of the Kuroshio onshore intrusion along the East China Sea shelf break: effect of the Kuroshio volume transport. *J Geophys Res Oceans* 119:6190–6209
- ✦ Liu N, Eden C, Dietze H, Wu D, Lin X (2010) Model-based estimate of the heat budget in the East China Sea. *J Geophys Res* 115:C08026
- ✦ Marsland SJ, Haak H, Jungclauss J, Latif M, Roske F (2003) The Max-Planck-Institute global ocean/sea ice model with orthogonal curvilinear coordinates. *Ocean Model* 5: 91–127
- ✦ Moss RH, Edmonds JA, Hibbard KA, Manning MR and others (2010) The next generation of scenarios for climate change research and assessment. *Nature* 463:747–756
- ✦ Oey LY, Chang MC, Chang YL, Lin YC, Xu FH (2013) Decadal warming of coastal China seas and coupling with winter monsoon and currents. *Geophys Res Lett* 40: 6288–6292
- ✦ Park WS, Oh IS (2000) Interannual and interdecadal variations of sea surface temperature in the East Asian marginal seas. *Prog Oceanogr* 47:191–204
- ✦ Sakamoto TT, Hasumi H, Ishii M, Emori S, Suzuki T, Nishimura T, Sumi A (2005) Responses of the Kuroshio and the Kuroshio Extension to global warming in a high-resolution climate model. *Geophys Res Lett* 32:L14617
- ✦ Schauer U, Beszczynska-Moller A (2009) Problems with estimation and interpretation of oceanic heat transport—conceptual remarks for the case of Fram Strait in the Arctic Ocean. *Ocean Sci* 5:487–494
- ✦ Sein DV, Mikolajewicz U, Gröger M, Fast I and others (2015) Regionally coupled atmosphere–ocean–sea ice–marine biogeochemistry model ROM. 1. Description and validation. *J Adv Model Earth Syst* 7:268–304
- ✦ Seo GH, Cho YK, Choi BJ, Kim KY, Kim BG, Tak YJ (2014) Climate change projection in the Northwest Pacific marginal seas through dynamic downscaling. *J Geophys Res Oceans* 119:3497–3516
- ✦ Soeyanto E, Guo X, Ono J, Miyazawa Y (2014) Interannual variations of Kuroshio transport in the East China Sea and its relation to the Pacific Decadal Oscillation and mesoscale eddies. *J Geophys Res Oceans* 119: 3595–3616
- ✦ Song J, Xue H, Bao X, Wu D and others (2011) A spectral mixture model analysis of the Kuroshio variability and the water exchange between the Kuroshio and the East China Sea. *Chin J Oceanology Limnol* 29:446–459

- Su J, Pan Y (1987) On the shelf circulation north of Taiwan. *Acta Oceanol Sin* 6:1–20
- ✦ Su J, Sein DV, Mathis M, Mayer B and others (2014) Assessment of a zoomed global model for the North Sea by comparison with a conventional nested regional model. *Tellus A: Dyn Meteorol Oceanogr* 66:23927
- ✦ Tang X, Wang F, Chen Y, Li M (2009) Warming trend in northern East China Sea in recent four decades. *Chin J Oceanology Limnol* 27:185–191
- ✦ Taylor KE, Stouffer RJ, Meehl GA (2012) An overview of CMIP5 and the experiment design. *Bull Am Meteorol Soc* 93:485–498
- ✦ Toggweiler JR, Russell J (2008) Ocean circulation in a warming climate. *Nature* 451:286–288
- ✦ Tseng C, Lin C, Chen S, Shyu C (2000) Temporal and spatial variations of sea surface temperature in the East China Sea. *Cont Shelf Res* 20:373–387
- ✦ Wang J, Oey LY (2016) Seasonal exchanges of the Kuroshio and shelf waters and their impacts on the shelf currents of the East China Sea. *J Phys Oceanogr* 46:1615–1632
- ✦ Wernberg T, Smale DA, Tuya F, Thomsen MS and others (2013) An extreme climatic event alters marine ecosystem structure in a global biodiversity hotspot. *Nat Clim Chang* 3:78–82
- ✦ Wu CR (2013) Interannual modulation of the Pacific Decadal Oscillation (PDO) on the low-latitude western North Pacific. *Prog Oceanogr* 110:49–58
- ✦ Wu CR, Hsin YC, Chiang TL, Lin YF, Tsui IF (2014) Seasonal and interannual changes of the Kuroshio intrusion onto the East China Sea Shelf. *J Geophys Res Oceans* 119: 5039–5051
- ✦ Wu L, Cai W, Zhang L, Nakamura H and others (2012) Enhanced warming over the global subtropical western boundary currents. *Nat Clim Chang* 2:161–166
- ✦ Xie SP, Hafner J, Tanimoto Y, Liu WT, Tokinaga H, Xu H (2002) Bathymetric effect on the winter sea surface temperature and climate of the Yellow and East China seas. *Geophys Res Lett* 29:2228
- ✦ Yang J, Liu Q, Xie SP, Liu Z, Wu L (2007) Impact of the Indian Ocean SST basin mode on the Asian summer monsoon. *Geophys Res Lett* 34:L02708
- ✦ Yeh SW, Kim CH (2010) Recent warming in the Yellow/East China Sea during winter and the associated atmospheric circulation. *Cont Shelf Res* 30:1428–1434
- ✦ Yu X, Wang F, Tang X (2012) Future projection of East China Sea temperature by dynamic downscaling of the IPCC_AR4 CCSM3 model result. *Chin J Oceanology Limnol* 30:826–842
- ✦ Yuan D, Hsueh Y (2010) Dynamics of the cross-shelf circulation in the Yellow and East China seas in winter. *Deep Sea Res II* 57:1745–1761
- ✦ Zhang J, Guo X, Zhao L, Miyazawa Y, Sun Q (2017) Water exchange across isobaths over the continental shelf of the East China Sea. *J Phys Oceanogr* 47:1043–1060
- ✦ Zhang Q, Hou Y, Yan T (2012) Inter-annual and inter-decadal variability of Kuroshio heat transport in the East China Sea. *Int J Climatol* 32:481–488
- ✦ Zhang X, Wang Q, Mu M (2017) The impact of global warming on Kuroshio Extension and its southern recirculation using CMIP5 experiments with a high-resolution climate model MIROC4h. *Theor Appl Climatol* 127:815–827
- ✦ Zhou F, Xue H, Huang D, Xuan J, Ni X, Xiu P, Hao Q (2015) Cross-shelf exchange in the shelf of the East China Sea. *J Geophys Res Oceans* 120:1545–1572

*Editorial responsibility: Oliver Frauenfeld,
College Station, Texas, USA*

*Submitted: February 21, 2019; Accepted: August 30, 2019
Proofs received from author(s): November 21, 2019*